Dynamics of Singlet Oxygen Molecule Trapped in Silica Glass, Studied by Luminescence Polarization Anisotropy and Density Functional Theory

Linards Skuja[*†], *Krisjanis Smits*[†], *Anatoly Trukhin*[†], *Florian Gahbauer*[‡], *Ruvin Ferber*[‡], *Marcis Auzinsh*[‡], *Laima Busaite*[‡], *Lukas Razinkovas*[§] , *Mažena Mackoit-Sinkevičienė*[§], *and Audrius Alkauskas*[§]

[†]Institute of Solid State Physics, Kengaraga 8, University of Latvia, Riga LV-1063, Latvia

[‡] Laser Centre, University of Latvia, 19 Raina Blvd., Riga LV-1586, Latvia

[§] Center for Physical Sciences and Technology (FTMC), Vilnius LT-10257, Lithuania

*email of the corresponding author: skuja@latnet.lv

Abstract

The lowest excited electronic state of the O_2 molecule, $a\ ^1\Delta_g$, the "singlet oxygen", is of utmost importance for photochemistry and photobiology. For O_2 trapped in silica glass, the lifetime of this state and the associated $a^1\Delta_g \longrightarrow X^3\Sigma_g^-$ photoluminescence (PL) is the longest known for O_2 in any condensed medium at room temperature. We studied the temperature dependence, decay kinetics and polarization anisotropy of this PL with 1064 nm excitation to the $a^1\Delta_g$ (v=1) state, as well as with excitation to higher energies. PL at this excitation shows non-zero polarization anisotropy at 295 K, which increases with cooling to 14 K. At variance, excitation to higher energies yields depolarized PL. Polarization data indicate weak electric dipole character of the emission of the spin- and parity-forbidden $a^1\Delta_g \longrightarrow X^3\Sigma_g^-$ transition, enabled by O_2 – SiO_2 cage interactions. Density functional theory calculations indicate that at low temperatures the rotation of O_2 is partially or fully frozen even in large silica voids. As the temperature increases, PL is increasingly depolarized by libration movement of O_2 molecules. Analysis of O_2 optical absorption in optical fibers allows one to obtain the absorption cross sections of $X \longrightarrow a$ and $X \longrightarrow b$ transitions of O_2 in SiO_2 glass and to evaluate both radiative and non-radiative rates of $a \longrightarrow X$ luminescence.

Introduction

The two lowest electronic excited states of free or matrix-isolated oxygen molecule O_2 are the metastable singlets ($a^1{}_g$ and $b^1\Sigma_g^+$), located at 0.97 eV and 1.62 eV above the triplet ground state ($X\ ^3\Sigma_g^-$), respectively (Fig. 1). O_2 molecules in the lowest excited $a\ ^1{}_g$ state are often referred as "singlet oxygen" or "$^1O_2$". They are of immense importance in photobiology [1], photodynamic cancer therapy [1–3], and photocatalysis [4]. Many reviews spanning decades of research are available, *e.g.* refs.[5–7]. The presence of $^1O_2$ is commonly monitored by the ~1270 nm luminescence band caused by the $a(v{=}0) \longrightarrow X(v{=}0)$ transition (Fig. 1, ν denotes the vibrational quantum number). In free O_2 this transition is forbidden by spin and symmetry selection rules. The luminescence is observable only because these selection rules are relaxed by perturbations from the surroundings. The theoretical models of the enhancement of radiative and non-radiative

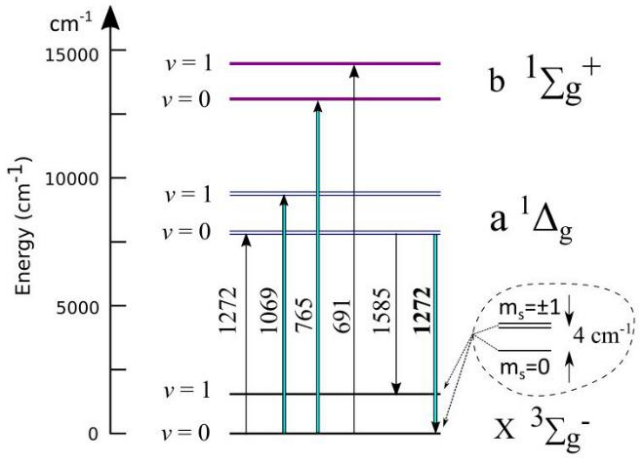

Fig.1. Optical absorption and luminescence transitions observed [8–10] in interstitial O_2 molecule embedded in glassy SiO_2. The transitions studied in this work are indicated by bold arrows. The transition wavelengths are in nm. Zero-field splittings (≈ 4 cm^{-1}) [11] of both the triplet ground state X (v=0) and its first vibrational (v=1) sublevel are shown.

transitions were recently reviewed [11,12]. Despite the external perturbations, the absorption transitions (Fig.1) remain extremely weak, therefore in most cases the luminescence is excited indirectly, via energy-transfer from an activator. More recently, a direct photoexcitation via $X \longrightarrow a$ and $X \longrightarrow b$ transitions has been employed [13] and the absorption cross sections of these two transitions in different solvents have been evaluated [14,15]. The option of enhancing $X \longrightarrow b$ transition by surface plasmon resonance was recently explored [16].

Apart from the fields of photobiology and photocatalysis, singlet and triplet O_2 plays an important role in the physics of glassy SiO_2 (g-SiO_2, silica glass), the basic material for fiber optical waveguides and ultraviolet (UV) optical components. Interstitial O_2 molecules strongly affect their optical properties and radiation toughness [17]. They are introduced in g-SiO_2 by manufacturing [18], high-T diffusion [19], dimerization of O atoms, displaced from SiO_2 network by nuclear irradiation [8] or by fs laser pulses [20], or by electric field applied at high temperatures [21]. While the interstitial O_2 is detrimental to UV applications of g-SiO_2 [17,22], it is found to increase the radiation toughness of optical fibers in the near-infrared range [23]. Luminescence of singlet O_2 provides means for high-sensitivity monitoring of O_2 concentration in g-SiO_2 [24,25] and has been used to study O_2 diffusion, isotope exchange with the glass network, or defect creation in bulk g-SiO_2[10] and SiO_2 nanoparticles [9].

Comparison of the basic properties of interstitial O_2 in g-SiO_2 with the large base of data on $^1O_2$ in solvents and solid matrices reveals an outstanding feature: the lifetime of the $a^1{}_g$ state of O_2 in g-SiO_2 $\tau \approx 0.82$ s, [26] is the longest observed for O_2 in any condensed medium at room temperature. $^1O_2$ lifetimes in liquids are typically in the microsecond range with an exception of only few halogenated solvents, where they are up to few hundreds of milliseconds: (*e.g.*, τ= 128 ms for CCl_4 , 309 ms for perfluorodecalene $C_{10}F_{18}$ [27]) . Lifetimes of $^1O_2$ in different liquids are compiled in ref.

[7] (p.31) and in the supplement of ref.[11]. $^1O_2$ lifetimes in organic polymer matrices are typically in the range of 5 μs – 100 μs (ref.[7], p.34); they are significantly higher in fluorocarbon polymers, e.g., 320 μs in nafion matrix [28] In nanoporous alumosilica and zeolite nanoparticles the $^1O_2$ lifetimes are generally into the same range (3 μs to 64 μs)[29]. The shortening of $^1O_2$ lifetimes in these solids or liquids is due to a much stronger non-radiative quenching, compared to the case of $^1O_2$ in g-SiO_2.

The most common non-radiative quenching mechanism of $^1O_2$ is electronic-to-vibrational (e-v) energy transfer to vibrationally-excited electronic ground state of O_2. The energy difference between the 0-th vibrational level of the excited state ($^1\Delta_g$, v=0) and vibrationally excited ground state ($^3\Sigma_g^-$, v=m, m>0) is absorbed by vibrations of some "deactivator species" Y. The energy balance is given by: [5,27]

$$O_2\ (^1\Delta_g, v=0) + Y(v'=0) \rightarrow O_2\ (^3\Sigma_g^-, v=m) + Y(v'=n) + E_{mn} \quad (1)$$

where m and n are vibrational quantum numbers of m-th and n-th vibrational excited states of O_2 and Y, and E_{mn} is the "off-resonance" difference energy, not absorbed by these vibrational modes. It is provided or absorbed by some low-energy excitations of the surroundings.

A long lifetime of $^1O_2$ is highly desired in photodynamic therapy applications where a photosensitizer is encapsulated in a nanoparticle, protected from reactants by a silica shell, and photogenerated $^1O_2$ must traverse the shell to its target before it is quenched. The lifetime of $^1O_2$, strongly confined in the interstitial voids in g-SiO_2 glass network, is ~10^4 times longer than τ=64 μs, measured for porous SiO_2 [29]. The largest source of this difference is evidently the presence of ≡Si–O–H groups on the internal surfaces of porous SiO_2. They are known as very efficient quenchers of $^1\Delta_g$ state with m=0, n=2 in eq.1.

The second cause of the more rapid quenching of $^1O_2$ in porous SiO_2 could be the additional rotational and translational degrees of freedom, available for O_2 in the porous SiO_2 as compared to

O_2, tightly confined in g-SiO_2 voids, which have an estimated average diameter of ≈5 Å [30]. These degrees of freedom could provide the E_{mn} in eq.1 and thus enhance luminescence quenching.

Another point of interest in interstitial O_2 is its ground-state magnetic momentum, which can be optically modulated by excitation to the $^1\Delta_g$ state. O_2 has been used as a test magnetic molecule for diamond NV-center based nanoscale magnetometry [31]. For this type of experiments, the dynamic properties of O_2 in SiO_2 are of interest.

The main aim of the present study is a better understanding of the conditions which provide the outstandingly long lifetime of $^1O_2$ in silica. We studied the thermal quenching of $^1O_2$ and luminescence polarization anisotropy. The latter, as well as its temperature behavior, gives information as to whether interstitial O_2 can rotate in the voids of g-SiO_2. We find that the rotational motion of O_2 in silica voids is largely hindered, thus explaining polarization anisotropy and also the long luminescence lifetimes.

Methods

Samples

Typical g-SiO_2 does not contain interstitial O_2 in measurable concentration (>10^{14} cm^{-3}). Two special samples, obtained by oxidation of $SiCl_4$ in oxygen-excess conditions were used. They had similar, albeit not entirely equal concentrations (in units of 10^{16} cm^{-3}) of bound hydroxyl ≡SiOH groups (6 and 5.3), interstitial Cl_2 molecules (51 and 79) and interstitial O_2 (29 and 43), respectively. The O_2 concentrations were determined with ±20% accuracy by the intensities of singlet O_2 PL intensities relative to Raman bands, pre-calibrated[25] by comparison to O_2 thermal desorption data. Sample dimensions were 5×10×12 mm^3, all 6 faces were optically polished.

Instrumentation and measurement methods

For a direct excitation of $^1O_2$ luminescence, CW mode lasers, modulated by electro-mechanic shutter were used: (1) 1064 nm diode-pumped Nd-YAG laser (LSR1064H, max. power 3 W) with Edmund Optics (EO) laser line cleanup filter 68-859, (2) 766 nm diode-laser (Leading Tech ADR1805, spectrum full width at half maximum, FWHM=2 nm, max. 600 mW) with 950 nm shortpass filter EO 64-328. The wavelengths of the laser light, 1064 nm and 766 nm roughly correspond to $X \longrightarrow a$ (v=1) and $X \longrightarrow b$ (v=0) transitions (Fig. 1). The laser light was focused on the sample by F=210 mm lens.

$^1O_2$ PL spectra were recorded using AMKO LTI 200 mm monochromator with 600 l/mm grating blazed at 1200 nm and Hamamatsu R5509-43 liquid N_2-cooled photomultiplier tube (PMT). Spectral resolution was 8 to 16 nm. Time-resolved PL spectra or kinetics were obtained in photon counting or analog (photocurrent) modes.

PL polarization anisotropy was obtained in the usual "L" geometry [32], featuring horizontal and mutually perpendicular excitation and emission beams. The excitation beam was polarized with E-vector in either vertical (V) or horizontal (H) directions. The $^1O_2$ PL beam was observed at right angle with polarization filter turned in (v) or (h) directions. The ratio I_{Vh}/I_{Vv} * between the intensities of horizontally (I_{Vh}) and vertically (I_{Vv}) polarized emission, observed using vertically polarized excitation beam, was measured. To obtain the correction for the polarization-dependent instrument

* The 1st index (capital H or V) denotes the excitation polarization direction, the 2nd one (lower case h or v) – the PL emission polarization direction.

response, the ratio I_{Hh}/I_{Hv} was measured with horizontally polarized excitation light. The PL polarization anisotropy r [*]) was then calculated [32]:

$$= \frac{1-}{1+2}, \qquad (2)$$

where $R = (I_{Vh}/I_{Vv})\,(I_{Hv}/I_{Hh})$ is the true intensity ratio, obtained by dividing the measured ratio I_{Vh}/I_{Vv} by the instrument response I_{Hh}/I_{Hv}.[†]

For correct polarization anisotropy measurements of a weak PL emission under high-power excitation, it is of utmost importance to suppress detection of any excitation light scattered from the sample or optical elements, since it is strongly polarized and can distort the results. Therefore, for an accurate measurement of r, time-resolved mode was used as an alternative to spectral scans. After exciting the sample for 3 s, the laser beam was blocked by a mechanical shutter and the PL decay signal was collected for 5 s. It was averaged over many cycles by photon counter or analog waveform recorder. To minimize the instrumentation-induced polarization distortions (I_{Hh}/I_{Hv}), in

---

[*] For historical reasons, polarization degree P =(1-R)/(1+R) is often alternatively used. It is related to r as $P=3r/(r+2)$. Usage of r is preferred, since it simplifies many polarization-related calculations [32].

[†] Obtaining the "instrument function" as I_{Hh}/I_{Hv} is accurate only for transitions, excited by the *electric* field component of the excitation beam. For I_{Hv} and I_{Hh} this component is directed along the observation axis and creates axially symmetric ensemble of excited PL centers, for which I_{Hh} must be equal to I_{Hv}. Any deviations are due to instrumental effects. This is correct in vast majority of cases. It may be incorrect for *magnetic* dipole transitions, where I_{Vv}/I_{Vh} should be used instead. We checked that I_{Hh}/I_{Hv}, measured with 766 nm excitation at 295 K is within 1.5% of ratio I_h/I_v measured using depolarized tungsten lamp instead of luminescent sample as a light source.

the case of time-resolved polarization measurements the emission monochromator was removed, and additional filters were used to block any light outside the $^1O_2$ PL emission region. The emitted light was collimated by BK7 glass aspheric lens, and then sequentially filtered by 4 filters: 1) interference 1100 nm long-pass edge filter (Edmund Optics EO 66-241); 2) interference bandpass filter (1250-1300nm, EO 87-865); 3) silicon wafer of thickness 0.5 mm; 4) wire-grid polarizer (Thorlabs WP25M-UB) to analyze the polarization of the emitted light. The light was then focused on PMT by BK7 glass lens. The polarization of the excitation light was rotated by a half-wave plate (1064 nm) or by rotating the laser case (766 nm).

For room-T to 14 K range measurements the sample was placed in vacuum in closed-cycle He refrigerator; measurements at higher *T* were performed in air atmosphere. During the low-*T* measurements, it was verified by changing the laser intensity that sample heating by laser does not significantly affect the results.

Calculation methods

To support the experimental findings, we have performed electronic structure calculations based on density functional theory (DFT). The principal task of calculations is to study rotational motion of interstitial O_2 in glassy silica. Calculations have been performed using the VASP code [33,34]. We have employed the semi-local GGA (generalized gradient approximation) density functional of Perdew-Burke-Ernzerhof (PBE) to describe the electronic structure [35]. We have used the projector-augmented-wave approach[36] with a plane-wave energy cutoff of 400 eV to describe electronic wavefunctions. The Brillouin zone was sampled at the Γ point. In our calculations the O_2 molecule is charge-neutral with a spin *S=1*. Our principal interest is to determine the potential energy surface for the rotation of O_2 in silica, and we expect the potential energy surfaces for singlet and triplet oxygen to be rather similar, since they have the same nominal electron configuration and therefore similar electronic structure. This premise is supported by the negligible Stokes shift in the PL

spectra and by calculated close polarizabilities in both states. The polarizability in the excited singlet *a* state is estimated as ~93% of that in the ground state of O_2 in organic solvents[37] and ~95% [37] or 96%[38] for gaseous O_2.

It is well documented [39–41] that the behavior of O_2 in various forms of silicon dioxide (e.g., α-quartz, β-cristobalite, and various forms of amorphous SiO_2) can be very different. One of the main factors determining this difference is the volume of interstitial voids. These volumes are on average larger in amorphous SiO_2 than in crystalline SiO_2. Thus, it is important to use representative structures of *a*-SiO_2 in computational studies of O_2 in SiO_2. In this work we have employed the 144-atom model developed by Bongiorno and Pasquarello [39,40]. The model has been obtained via molecular dynamics simulations by quenching the amorphous structure from the melt by first employing empirical force fields and then using density functional theory to relax the final structure. The model consists of a random network of corner-sharing tetrahedra, and reproduces the most important parameters of experimental amorphous SiO_2 structures, most crucially, the density ρ=2.2 g/cm^3, as well as pair distribution functions between different atom types (Si-Si, O-O, and Si-O). More detailed information is provided in Refs. [39,40].

Results

Temperature dependence of luminescence kinetics

The decay kinetics of luminescence, excited at 766 nm, measured in the 15 K-503 K temperature range are shown in Fig. 2. The emission intensity was measured with monochromator set at the maximum of $^1O_2$ PL band (1272 nm) and spectral resolution 10 nm. Even at the highest measurement temperature (503 K) the emission was only partially quenched (Fig.3, inset). Measurements at higher T's were hindered by an increasingly strong thermal radiation from sample surroundings swamping the PL signal. The decay kinetics is close to mono-exponential, in accord

with the previous observations[26]. The decay constant τ was obtained by least-squares fits (Fig. 2) drawn over the dynamic range of e^2, corresponding to the decay of ≈85% of all excited O_2 molecules. The temperature dependences of τ and of the luminescence intensity are shown in Fig.3. The low-T limit value of τ, 1115 ms, denoted as τ_0 in Fig. 3, was slightly excitation wavelength-dependent. With the 1064 nm excitation τ_0≈1230 ms. A higher value, τ_0 =1350 ms was observed in some g-SiO_2 samples, where O_2 was excited by energy transfer from activator (to be published elsewhere).

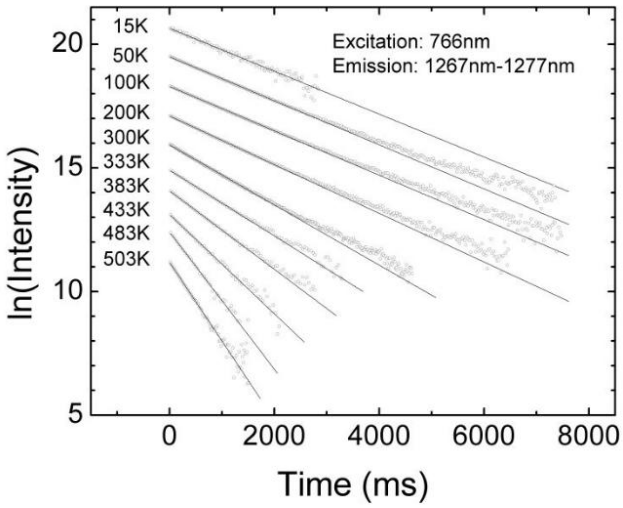

Fig. 2. Decay kinetics of $^1O_2$ luminescence in dry silica glass in temperature range 15 K-503 K. Exponential fits to the initial parts of kinetics, corresponding to intensity decay e^2 times, are shown by solid lines.

The temperature dependence of PL intensity at low T's, while generally following the changes of τ, was additionally affected by the decreasing widths of $X \longrightarrow a$ (v=1) and $X \longrightarrow b$ excitation bands. This changes the efficiencies of excitation by 1064 nm and 766 nm lasers, whose wavelengths do not exactly match the respective excitation maxima. Therefore, only the more reliable high-T part of the temperature dependence of PL intensity is presented (Fig.3, inset).

Fig.3. Arrhenius plot according to eq.(3), showing activation energy of ≈ 1550 cm^{-1} for the high-temperature non-radiative quenching of O_2 PL. Inset shows the measured temperature dependence of the PL intensity and of the PL decay constant.

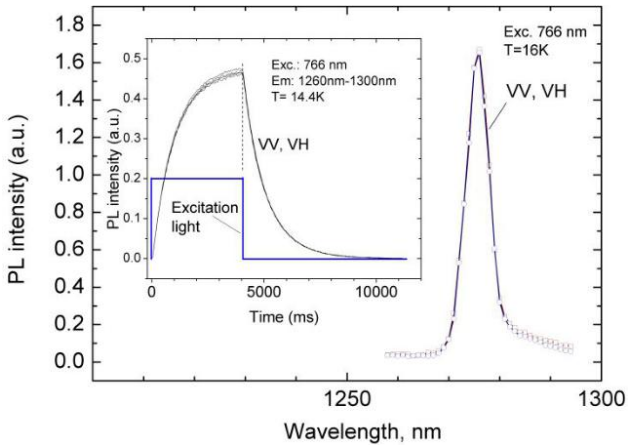

Fig.4. $^1O_2$ luminescence spectra of vertically (Vv) and horizontally (Vh) polarized components, excited by vertically (V) polarized 766 nm light at T=16 K. Inset shows Vv and Vh component intensities, measured in time-resolved mode after cut-off of the excitation light. No measurable polarization is detected.

Luminescence polarization anisotropy

When excited by the 766 nm laser, the polarization anisotropy *r* (eq. 2) of $^1O_2$ PL is zero within the measurement accuracy (~0.6%). *r* does not increase at low temperature (~15 K): the intensities

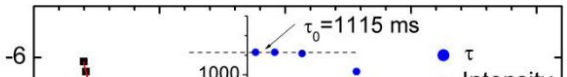

of the vertically (*Vv*) and horizontally (*Vh*) polarized components remain equal (Fig. 4), whether measured in the spectrally resolved or time-resolved (Fig. 4, inset) modes.

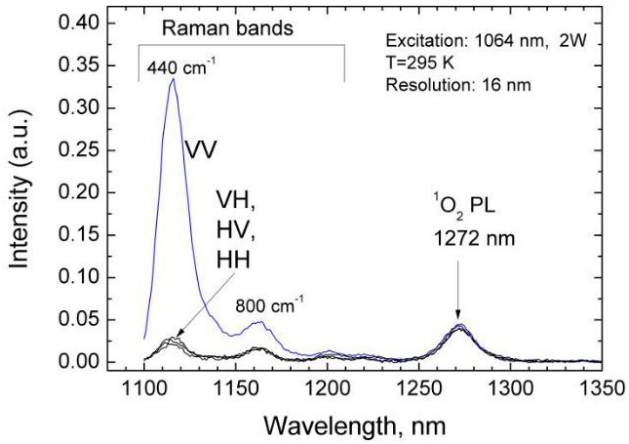

Fig.5. Strongly polarized fundamental 440 cm^{-1} and 800 cm^{-1} Raman bands and $^1O_2$ luminescence spectra of silica glass with embedded O_2 molecules, measured with linearly polarized 1064 nm excitation for Vv, Vh, Hv and Hh polarization components.

Room-temperature excitation at 1064 nm (Fig. 5) gives rise to strongly polarized (*Vv*) g-SiO_2 fundamental Raman bands and to a weaker $^1O_2$ PL band with *Vv* polarized component having slightly higher intensity as compared to *Vh*, *Hv* and *Hh*-polarized spectra. However, the intensity difference between *Vv* and other 3 polarizations only marginally exceeded the measurement error. Therefore, the polarization anisotropy and its temperature dependence were further measured, using the more accurate time-resolved mode (Fig. 6). At each temperature, 4 identical sets of decay kinetics were measured, each set comprising measurements at 4 polarization configurations (*Vv*, *Vh*, *Hv*, and *Hh*), and the respective *r* values were calculated from them by eq. (2). The temperature dependence of their average $r=r(T)$ and its dispersion are shown in Fig. 6. Insets to Fig. 6 show the intensities of PL decay at 4 polarization configurations at 295 K and 14.6 K. It is most evident in the 14.6 K measurement that the *Vv*-polarized component is more intense, while *Vh*, *Hv* and *Hh* components have smaller and mutually equal intensities.

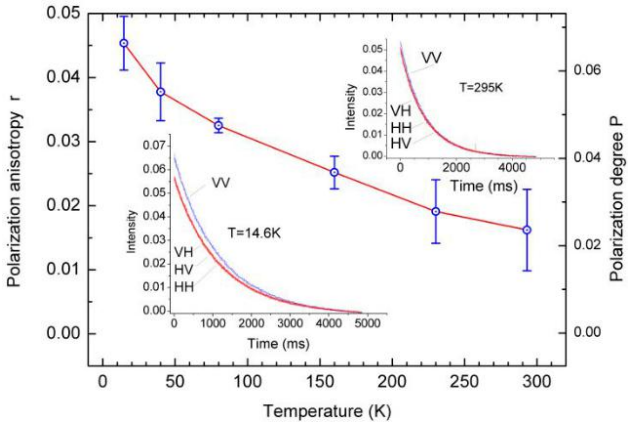

Fig.6. Temperature dependence of polarization anisotropy of $^1O_2$ luminescence measured by recording the luminescence decay intensities, integrated over 20 to 1840 ms interval after cut-off of the polarized 1064 nm excitation light. Insets show luminescence transients at T=14.6 and 295 K. Vh, Hv and Hh-polarized components have equal intensities, lower than the Vv component intensity.

The polarization anisotropy *r* is clearly non-zero (+1.6%) at room temperature and reaches +4.5% at 14.6 K (Fig. 6). We checked that *r* does not change significantly during the PL decay (Fig. 7). Both *Vv* and *Vh* component decay similarly at least within the first 5 seconds. The slight difference between the fitted decay constants is within the error limits.

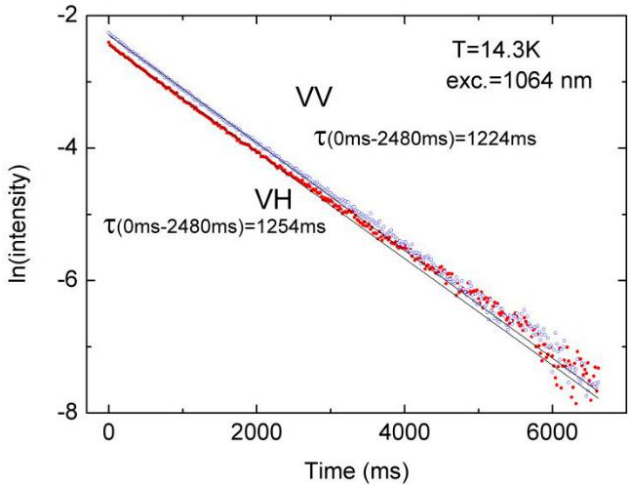

Fig.7. Comparison of decay kinetics of vertically (Vv) and horizontally (Vh) polarized components of $^1O_2$ luminescence under vertically polarized excitation at 1064 nm. The emission was collected in 1250 nm-1300 nm spectral range. Solid lines are fits to semilog scale data in 0 ms - 2480 ms range.

Calculation of interstitial O_2 rotation

g-SiO_2, as an amorphous material, is characterized by a wide distribution of interstitial voids [30]. Volumes of the voids extend from approximately 25 $Å^3$ (radius 1.8 Å) to more than 250 $Å^3$, (radius ~4Å) [39–41], with the average volume being about 65 $Å^3$ (radius 2.5 Å) [30]. In contrast to g-SiO_2, the distribution of voids in α-quartz is very narrow, with an average volume of ≈33 $Å^3$ [39,40]. The volume of interstitial voids has direct consequences on the energy of the interstitial O_2 molecule. It has been shown that there is a clear inverse correlation between the volume of the void and the energy of O_2 incorporation[39,40]. In particular, this energy is ~3.5 eV for O_2 in α-quartz (volume 33 $Å^3$), and reaches nearly zero when the volume becomes larger than about 125 $Å^3$ [40]. Thus, under thermal equilibrium conditions O_2 in g-SiO_2 will reside in voids having the largest volumes. High

incorporation energy of O_2 in α-quartz is probably one of the reasons why, to the best of our knowledge, interstitial O_2 has never been observed in undamaged lattice of α-quartz.

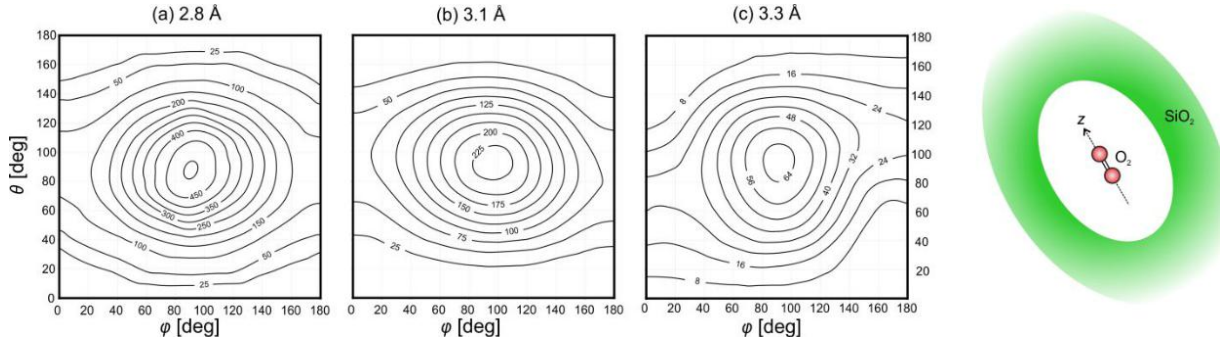

Fig. 8 . Contour plots describing the rotation barriers for an O_2 molecule in voids with radii of 2.8, 3.1 and 3.3 Å. The energy values are in meV.

Instead of trying to perform an extensive statistical analysis, our main goal is to answer the following qualitative question: is the rotation of O_2 molecules in large voids, where they are likely to be under thermal equilibrium, frozen, hindered, or nearly free? In order to answer it, we have chosen three large voids with volumes 92 $Å^3$ (radius 2.8 Å), 125 $Å^3$ (radius 3.1 Å), and 150 $Å^3$ (radius 3.3 Å), all of which are larger than the average void in silica. To investigate the rotational motion of O_2 in these voids, we calculated the potential energy surface of the O_2 molecule as a function of the spherical angles ϑ, φ. As the first step, the potential energy surface was calculated by keeping the lattice frozen, and only the molecule was allowed to rotate. The resulting contour plots of the potential energy surfaces $(\ , \ )$ for the three voids are shown in Fig. 8. Due to the inversion symmetry of the molecule, the potential has the property $(\ ,) = (\ - \ , \ + \ )$, and thus it is sufficient to take the range of φ from 0 to 180 degrees. In the plot the value ϑ=0 corresponds to the lowest-energy orientation of the molecule. Allowing the lattice to relax for each

orientation of the molecule lowers the energies by at most 15%, and therefore we discuss the results of a frozen lattice here.

The calculated potential energy surface helps understanding the behavior of the rotational motion of the molecule at different temperatures. Let us first discuss the behavior of the molecule in the void with radius 3.1 Å (Fig. 8(b)). At cryogenic temperatures $\ll 10$ meV, and the orientation of the O_2 molecule is essentially frozen. At room temperature ≈ 25 meV, and now the

orientation of the molecule can exhibit vibrational motion in the solid angle of $\lesssim 1$, corresponding to $\lesssim 30$ degrees. The barrier for the molecule to change from 0 to 180 degrees is ~80 meV. However, the total rotational motion of the molecule is partially hindered up to ≈ 200 meV (the highest barrier in Fig. 8(b)), that means, under essentially all experimental conditions.

If we consider a smaller void (Fig. 8(a), radius 2.8 Å), the barriers are yet higher: the rotational motion of the molecule is frozen at low temperatures, and only some wobbling around the equilibrium orientation is allowed at room temperature. As the volume of the voids increases, the rotational barriers tend to decrease. *E.g.*, for voids with radius 3.3 Å (Fig. 8(c)), those barriers can become as small as 20 meV. This means that the rotational motion is still frozen at low temperatures, but as the temperature approaches room temperature, molecules experience substantial libration motion.

While, as discussed above, an exhaustive statistical analysis is not the aim of the present paper, the analysis of the behavior of O_2 molecules in a few representative voids suggests that rotational movement of O_2 molecules in voids, in which they are likely to reside, is frozen at low temperatures, and partially allowed at room temperature.

To make sure that our computational setup is reliable regarding the rotational motion of molecules in g-SiO_2, we have performed identical calculations for the H_2 molecule. There are

strong indications from Raman scattering studies that H_2 rotates nearly freely in g-SiO_2 at room temperature [42]. Indeed, we find that, *e.g.*, the highest barrier of rotation of H_2 inside the 3.1 Å radius void in g-SiO_2 is ~5 meV, compared to ~200 meV for the O_2 molecule. This means that the H_2 molecule indeed rotates nearly freely at room temperature, in agreement with the experiment (Ref. [42] and Supplement B).

Discussion

Lifetime and quantum yield of singlet O_2 in glassy SiO_2

The decay constant τ_{meas} of $^1O_2$ PL in g-SiO_2, measured at 766 nm excitation, increases from ~860 ms at 295 K to the "saturation value" 1115 ms, observed at temperatures below 80 K (Fig. 3). The saturation value, obtained with 1064 nm excitation is slightly different ($\tau_{meas}\approx$1230 ms). This difference is most likely explained by static site-to site variations of O_2 sites in glassy matrix in conjunction with site-selective excitation: the ensembles, excited by 766nm and by 1064nm are evidently different. It gives a rough estimate of the disorder-induced spread of τ_{meas} values. The low-T saturation of τ_{meas} values is typical for most luminescence centers, where T-dependent non-radiative process with rate $1/\tau_{nr}$ competes with (usually less T-sensitive) radiative transitions, having rate $1/\tau_{rad}$:

$$\frac{1}{\quad} \quad \frac{1}{\quad} \quad \frac{1}{\quad} \qquad (3)$$

Our measured lifetimes are ≈1.6 times longer than those reported for $^1O_2$ in O_2-saturated Aerosil nanoparticles (460 ms and 700 ms at 295 K and 10 K, respectively)[43]. Assuming that the temperature-dependent non-radiative rate is described by the Arrhenius-type expression $1/\tau_{nr}\sim\exp(-E/k_BT)$, the activation energy E can be obtained as the slope of the plot of

$\ln(1/\tau_{meas}-1/\tau_0)$ vs. $1/T$, where τ_0 is the measured decay constant in the low-temperature limit. Assuming τ_0=1115 ms (Fig. 3, inset), the activation energy of ≈1550 cm^{-1} is obtained for the high-temperature thermal quenching (Fig.3). This energy is well above the highest fundamental vibration mode of g-SiO_2(~1200 cm^{-1}) and close to the vibration energy of O_2 molecule embedded in SiO_2: 1549 cm^{-1} in the $X\ ^3\Sigma_g^-$ (ground) state [8] and 1493±20 cm^{-1} in the $a\ ^1{}_g$ excited state [9]. That might indicate that the mechanism of high-temperature quenching of $^1O_2$ PL involves the activation of O_2 vibration modes.

As Fig. 3 demonstrates, the effective activation energy changes in the low-temperature region. However, the estimate of the PL quenching activation energy in this region, E=380 cm^{-1} (Fig. 3), is only tentative at best: it is based on just 2 data points and it is very sensitive to the choice of τ_0, which shows slight excitation wavelength dependence (see the Results part). Presently it can be only noted that: (i) similar value of low-T activation energy, E =340±40 cm^{-1} was obtained for O_2 in Aerosil particles [43]; (ii) this energy is close to the energy of the main Raman-band in g-SiO_2 (200...500 cm^{-1}, see, *e.g.*, ref. [24]); (iii) coupling to SiO_2 vibration modes is demonstrated by phonon sidebands in high-resolution $^1O_2$ PL spectra [8], showing that the involvement of the SiO_2 phonons in non-radiative decay is plausible.

It has been shown that the radiative rate of $^1O_2$ PL can also be temperature-dependent[44]. In the present case, however, the PL T-dependence in the high-T region is dominated by the change in non-radiative rate, since the intensity is proportional to the measured decay constant τ_{meas}, (Fig.3, inset) as predicted by eq. 3. This proportionality can not be proved in the low-T region, because reliable data on intensity T-dependence are not available.

The measured low-temperature decay constant τ_0 (1115 ms, Fig.3) is significantly smaller than the decay constant τ_{meas} ≈2150 ms, measured at *room* temperature for isotope-enriched ^{18}O-^{18}O

molecules in g-SiO_2[45]. Evidently, the radiative lifetime τ_{rad} of $^1O_2$ in g-SiO_2 must be at least 2150 ms. Assuringly, this lifetime is calculated to be around 3000 ms in the next section of the present paper; and it is estimated between 0.7 and 5 s for O_2 dissolved in different liquids (Table 2).

The difference between τ_0 and τ_{rad} ($\tau_{rad}/\tau_0 > 2$) indicates that a significant thermally non-activated quenching persists even at 15 K, and the PL quantum yield $\eta=\tau_0/\tau_{rad}$ is lower than ≈0.5 at T=15 K. Adopting the estimate of $\tau_{rad} \approx 3000$ ms would yield $\eta=0.37$ at T=15 K and $\eta= 860/3000 \approx 0.29$ at room temperature. It is unlikely that the radiative rate $1/\tau_{rad}$ for $^1O_2$ in SiO_2 could be much lower than the values listed in Table 2, therefore the luminescence quantum yield τ_0/τ_{rad} of $^1O_2$ in g-SiO_2 should be surely larger than 0.1. To the best of our knowledge, it is then the largest reported quantum yield for $^1O_2$ PL in solids at room temperature.

O_2 absorption cross sections and $^1O_2$ radiative lifetime in glassy SiO_2

Absorption cross sections σ of O_2 $b \longrightarrow X$ and $a \longrightarrow X$ transitions are extremely low, and for O_2 in various solutions it has been possible to measure them only indirectly, by quantifying the photochemical effects of singlet oxygen, created by direct $X \longrightarrow a$ or $X \longrightarrow b$ photoexcitation. Using this technique, σ for O_2 in different solvents were recently re-examined in Ref. [14].

Fortunately, g-SiO_2 is peculiar not only as the matrix providing the longest $^1O_2$ lifetime, but also as a material for fiber optical waveguides, which due to their typically long optical paths are sensitive to weak absorptions. Surprisingly, our analysis of literature data shows that σ for *X-a* and *X-b* transitions can be obtained *directly*, by supplementing the data on absorption of O_2 in optical fibers, published more than two decades ago [18,46] with later spectroscopic work [24,25], which allows to determine in hindsight the concentration of O_2 in these fibers (see supplement S1 for spectra and for details of their processing).

In optical fibers, produced in oxygen-rich conditions, two sharp optical absorption lines have been observed [46] : one at 1273 nm and the other at 765 nm (see Supplement, figure S1). Their amplitudes and full widths at half maximum (FWHM) are listed in Table 1 (denoted as "Experiment A"). The origin of these two lines was initially unidentified, however, their positions and small FWHM's clearly show that they are due to $X \longrightarrow a$ and $X \longrightarrow b$ transitions of O_2 in silica. They yield the ratio between the $X \longrightarrow a$ and $X \longrightarrow b$ absorption intensities (integrals I of absorption bands): $I_{1272nm}/ I_{765nm}=2.7\pm0.3$. Note that due to an extremely low absorption cross-section, requiring km-long samples, direct measurements are only possible in optical fibers, making such experiments unique.

The 765nm band in optical fiber was subsequently assigned to O_2 [18]. This assignment was proved by observing the sharp Raman line of interstitial O_2 at 1549 cm^{-1} and the 765 nm optical absorption band (Figs. S4 and S5 in Supplement) in *the same* optical fiber (Table 1, Experiment "B "). However, the concentration of O_2 in that optical fiber was not known. Our later work [24,25] allows to determine the absolute concentration of O_2 in g-SiO_2, using the intensity of the O_2 Raman band relative to the intensities of fundamental g-SiO_2 Raman bands. Hence, the concentration of O_2 in the fiber, studied in experiment "B"[18] can be determined in hindsight (2.4×10^{17} O_2/cm^3, Table 1). Further, by comparing the 765 nm absorption band integrals, the concentration of O_2 in the fiber used in Experiment "A"[46] is calculated (Table 1). Since O_2 $X \longrightarrow a$ and $X \longrightarrow b$ absorption bands are clearly visible in this fiber and their intensities α can be measured, their peak absorption cross sections $\sigma=\alpha/[O_2]$ can now be finally obtained after a slight correction for lower spectral resolution in Experiment B (see Supplement and footnote (c) under Table 1). Table 2 provides a comparison between the obtained σ values for O_2 in g-SiO_2 and O_2 in different organic solvents. They are reasonably similar. The accuracy of the cross sections for g-SiO_2 calculated in this paper (Tables 1, 2) is limited by the accuracy, with which numerical values can be extracted from the published

absorption and Raman spectra of the optical fibers [18,46] . Repeating these experiments with dedicated O_2 -loaded optical fibers would provide a way of accurate direct measurement of O_2 $X \longrightarrow a$ and $X \longrightarrow b$ absorption cross sections in g-SiO_2.

If the integral of absorption spectrum $\alpha(\ )$ and concentration N of absorbing/emitting species is known, then for narrow, not Stokes-shifted absorption/emission spectra the radiative transition (emission) rate $1/\tau_{rad}$ can be calculated by Perrin's formula (e.g., refs.[11,32])

$$\frac{1}{\tau_{rad}} = \frac{8\pi n^2 \tilde{\nu}_0^2}{\frac{g_{em}}{g_{abs}} N} \int_0^\infty \alpha(\tilde{\nu}) \, d\tilde{\nu} \qquad (4)$$

where n is the refractive index of the medium; $\tilde{\nu}_0$ is the central wavenumber (cm^{-1}) and g_{em} and g_{abs} are the relative weights of all statistically equivalent emission and absorption transitions at this wavenumber. These weights increase from 1 to 2 or 3, if the destination state is 2- or 3-fold degenerate, and they decrease below 1, if the effective population of the initial state is <1. Given the complex nature of the $X \longrightarrow a$ transition, and the fact that transitions become allowed only by perturbations from the surrounding host, the choice of g_{em}/g_{abs} is nontrivial, as already noted in Ref. [11]. Theoretical considerations indicate that $X \longrightarrow a$ transition in perturbed O_2 occurs mostly from the m_S=0 spin sub-level of the X ground state (Fig.1, see supplement of Ref.[11]). Transitions $X \longrightarrow a$ from the other two spin sub-levels ($m_S = \pm 1$) are not enhanced by the interaction with the host matrix, and their contribution to absorption is negligible. Therefore, the effective occupancy of the ground level for the $X \longrightarrow a$ absorption transition is ~1/3 at the room temperature, when all three spin sublevels are almost equally populated (zero-field splitting is 4 cm^{-1}, much smaller than kT). On the other hand, the $X \longrightarrow a$ absorption intensity is enhanced by factor 2 because the upper (spin singlet) level $a^1{}_g$ is orbitally two-fold degenerate. Together this yields $g_{abs} = 2/3$ for the $X \longrightarrow a$ transition. Conversely, for the reverse $a \longrightarrow X$ transition the statistical weight $g_{em} = 1$, since the only allowed

transition is to m_S=0 sublevel. Hence the ratio g_{em}/g_{abs} = 3/2 can be used for eq. (4). Substituting this value, the absorption integral from Table I and the refractive index n=1.447 at 1272 nm in eq.(4) yields $1/\tau_{rad} = 0.336\ s^{-1}$ or $\tau_{rad} \approx 3.0$ s. The longest room-temperature lifetime of $^1O_2$ in g-SiO_2, reported in literature, is 2.1 s, measured for ^{18}O-^{18}O molecules [45]. Therefore the calculated τ_{rad} value, which is the upper limit for the experimentally observed lifetimes, is not unreasonable. The estimates of τ_{rad} of $^1O_2$ in solvents range from 0.3 to 5 seconds [5] (and see Table 2). In the present paper, the main sources of error are the uncertainties related to eq.(4) and the accuracy of the concentration estimates, which mainly depends on the accuracy of the published relatively weak 765 nm absorption band [18]. In any case, these data demonstrate that $X \longrightarrow a$ and $X \longrightarrow b$ transitions of $^1O_2$ can be directly studied with relatively high accuracy using O_2 –containing optical fibers. Such fibers are presently being developed for near-infrared applications in radiation environments [23] and for luminescent dosimetry applications [47].

Character of the 1272 nm radiative transition

Quantum mechanical considerations, regarding the character of the lower optical transitions in a free and perturbed O_2 have been recently summarized by Bregnhøj *et. al.* [11] Their analysis indicates that in a free O_2 molecule the strongest contribution to $a \longrightarrow X$ transition is given by magnetic dipole transition, while the additional contribution of electric quadrupole component is much weaker [11]. The forbidden electric dipole transition is, however, more sensitive to perturbations from the environment. When O_2 is perturbed by an external potential, the transition can acquire electric-dipole character and can become up to ~1000 more intense than the magnetic dipole component of $a \longrightarrow X$ transition in the same perturbed O_2 molecule [11].

The relation between the intensities of differently polarized PL components (Fig.6, left inset), with a more intense Vv component and less intense and mutually equal Vh, Hv and Hh components, is consistent with an electric-dipole character of the $a^1{}_g \rightarrow X\,^3\sum_g^-$ transition suggested in ref. [11].

The angular dependence of PL polarization anisotropy, expected in the case of electric quadrupole excitation and emission transitions [48] is different from the one, observed in our work. Such transitions should yield r= -2/7≈-0.286 when the polarization of the excitation beam is horizontal, and yield r=0, when the excitation beam is polarized vertically. This difference further confirms the electric-dipole character of $^1O_2$ PL in silica.

In the case of 766 nm excitation the situation is more complicated: the $X \rightarrow b$ excitation is predicted to have magnetic-dipole character [11], and after $b \rightarrow a$ relaxation, $a \rightarrow X$ luminescence transition occurs, which, as discussed above, has electric-dipole character. The present data indicate that the polarization anisotropy is strongly decreased in this case, and is close to zero within our current level of accuracy (r=0.6%).

Rotation of O_2 in silica glass

O_2 molecules are tightly confined in interstitial voids. An extrapolation of the temperature-dependence of the O_2 diffusion coefficient[19] to room temperature yields diffusion length $L=(6Dt)^{1/2}$ of only ≈ 0.02 Å in 1 second, indicating that $^1O_2$ does not hop to neighboring void during its ~1 s lifetime. However, in principle this does not exclude its rotation within the containing void. In contrast to the case of interstitial H_2 molecules in g-SiO_2[42], rotation-vibrational Raman bands of O_2 in g-SiO_2 have not been found [24]. The non-zero PL polarization anisotropy (Fig. 6) indicates a definite correlation between the orientations of O_2 molecule during the photo-excitation and during the emission, which occurs on average ≈1 second later. The molecule either stays in a single, fixed

orientation, or, at least, has one preferred orientation, where it spends the largest fraction of time. In any case, it does not leave the void. The observed behavior is evidently an average over the distribution of void sizes in SiO_2 glass.

The polarization anisotropy is given by:[32]

$$r = \frac{3\langle \cos^2 \alpha \rangle - 1}{2} \qquad (5)$$

where α is the angle between the directions of absorbing and emitting dipoles and $\langle \cos^2 \alpha \rangle$ denotes average of $\cos^2 \alpha$ over all possible α values. If these directions coincide (α=0), then r=0.4.

If the luminescent excited state is orbitally doubly degenerate, as is the case for $a^1{}_g$ state of O_2, PL is additionally depolarized even if the molecular axis direction is fixed. Due to the axial symmetry of the molecule, the absorption and emission dipole transitions from non-degenerate to degenerate state (X⟶a) and back must be polarized in plane, normal to molecular axis. Since all directions in this plane are equivalent, the absorbing and emitting dipoles in this case can assume any mutual angle α within this plane. The value of $\langle \cos^2 \alpha \rangle$ in this case is 0.5 and, according to eq.(5), r is reduced to 1/10. If, in addition, the direction of the O_2 molecular axis can change during the excited state lifetime, and therefore, the emission plane is tilted from the absorption plane by an angle ϑ_0 , then $\langle \cos^2 \alpha \rangle = (1+\cos^2 \vartheta_0)/4$ and, according to eq.(5), the resulting anisotropy is further decreased:

$$r = (3\cos^2 \vartheta_0 - 1)/20 \qquad (6)$$

For r = 4.5% at 14.6 K and 1.6% at 295 K (Fig. 6), eq.(6) yields "average" angles ($arc\ cos(\langle \cos^2 \vartheta_0 \rangle)$) of O_2 axis deviation between absorption and emission events $\vartheta_0 \approx 37°$ and $\vartheta_0 \approx 48°$, respectively. Note that the "baseline value", a completely chaotic tumbling of O_2 corresponds to $\vartheta_0 = \arccos(3^{-1/2}) \approx 55°$. While this result should be regarded as a merely qualitative one, it

may

give the idea of the magnitude of the fluctuation of O_2 molecular axis directions in interstitial voids of g-SiO_2.

Conclusion

The temperature-dependent polarization anisotropy of $^1O_2$ luminescence in g-SiO_2 and DFT calculations demonstrate that O_2 molecule does not rotate freely in interstitial voids and maintain a correlation between the absorption and emission polarization directions. The transitions between the ground state (X) and the lowest singlet state (a) have weakly allowed electric dipole character, in accord with the theoretical predictions [11].

The temperature dependence of $^1O_2$ PL kinetics and its comparison to the radiative lifetime of ~ 3 seconds, deduced by an analysis of the O_2 optical absorption in fiber optical waveguides, allows to estimate that the $^1O_2$ PL quantum yield is above 0.1. To our knowledge, this is the highest quantum yield for $^1O_2$ luminescence at room temperature in any condensed matrix. The PL is still not completely quenched at temperatures as high as 200°C and O-O molecular vibration probably participates in the thermal quenching process.

It is evident that the tight confinement of O_2 in g-SiO_2 interstitial voids helps to avoid the collisional quenching of excited $^1O_2$ and contributes to the record-long lifetime of $^1O_2$ at room temperature in g-SiO_2. However, it also slows down the diffusion of O_2. For applications in photobiology [7], where both long lifetimes and long diffusion paths of $^1O_2$ are desired, an optimization of the confinement degree may be useful and could be a subject for further studies.

Supporting Information Description

Analysis of the literature data on optical fiber waveguides, which yields optical absorption cross sections of the $X \rightarrow a$ and $X \rightarrow b$ transitions of O_2 molecule trapped in silica glass.

Raman spectra of gaseous H_2 and H_2 in silica glass, illustrating the rotation of H_2.

Acknowledgements

The support from M-ERANET project "MyND" is acknowledged. A. A., M. M-S., and L. R. were supported by the Research Council of Lithuania (grant M-ERA.NET-1/2015). Authors thank A. Pasquarello for providing the structures of the amorphous SiO_2 matrix for our computational work and K. Kajihara (Tokyo Metropolitan University) for valuable advice in PL kinetics measurements.

Figure Captions

Fig.1. Optical absorption and luminescence transitions observed [8–10] in interstitial O_2 molecule embedded in glassy SiO_2. The transitions studied in this work are indicated by bold arrows. The transition wavelengths are in nm. Zero-field splittings (≈ 4 cm^{-1}) [11] of both the triplet ground state X (v=0) and its vibrational (v=1) sublevels are shown.

Fig. 2. Decay kinetics of $^1O_2$ luminescence in dry silica glass in temperature range 15 K-503 K. Exponential fits to the initial parts of kinetics, corresponding to intensity decay e^2 times, are shown by solid lines.

Fig.3. Arrhenius plot according to eq.(3), showing activation energy of ≈ 1550 cm^{-1} for the high-temperature non-radiative quenching of O_2 PL. Inset shows the measured temperature dependence of the PL intensity and of the PL decay constant.

Fig.4. $^1O_2$ luminescence spectra of vertically (Vv) and horizontally (Vh) polarized components, excited by vertically (V) polarized 766 nm light at T=16 K. Inset shows Vv and Vh component intensities, measured in time-resolved mode after cut-off of the excitation light. No measurable polarization is detected.

Fig.5. Strongly polarized fundamental 440 cm^{-1} and 800 cm^{-1} Raman bands and $^1O_2$ luminescence spectra of silica glass with embedded O_2 molecules, measured with linearly polarized 1064 nm excitation for Vv, Vh, Hv and Hh polarization components.

Fig.6. Temperature dependence of polarization anisotropy of $^1O_2$ luminescence measured by recording the luminescence decay intensities, integrated over 20 to 1840 ms interval after cut-off of the polarized 1064 nm excitation light. Insets show luminescence transients at T=14.6 and 295 K. Vh, Hv and Hh-polarized components have equal intensities, which are lower than the Vv component intensity.

Fig.7. Comparison of decay kinetics of vertically (Vv) and horizontally (Vh) polarized components of $^1O_2$ luminescence under vertically polarized excitation at 1064 nm. The emission was collected in 1250 nm-1300 nm spectral range. Solid lines are fits to semilog scale data in 0 ms - 2480 ms range.

Fig. 8 . Contour plots describing the rotation barriers for an O_2 molecule in voids with radii of 2.8, 3.1 and 3.3 Å. The energy values are in meV.

Tables

Table 1. Absorption Cross Sections of $X \longrightarrow a$ and $X \longrightarrow b$ Transitions of O_2 in Silica Glass Optical Fibers, Obtained from Analysis of Published Data [18,24,25,46] .

	1272 nm ($X \rightarrow a$) band			765 nm ($X \rightarrow b$) band			[O_2] (O_2/cm^3)
Experi-ment	amplitude (db/km)	fwhm (cm^{-1})	integral db/km*cm^{-1}	amplitude (db/km)	fwhm (cm^{-1})	integral db/km*cm^{-1}	
A: [46]	15.11	105	1587	5.82	103	597	1.6×10^{18} *a)*
B: [18]				0.45	180	89	2.4×10^{17} *b)*
C [9]		93 (PL)			103 (PLE)		
D: [24]		86 (PL)					
peak σ *c)*	2.7×10^{-23} cm^2			0.84 × 10^{-23} cm^2			

a) O_2 concentration obtained relative to the experiment B by scaling the $X \rightarrow b$ absorption band integrals

b) O_2 concentration obtained by comparing the intensity ratio of the O_2 Raman line relative to the fundamental g-SiO_2 Raman band around 1600 cm^{-1} (Experiment B) with a similar ratio, measured in Experiment D in a sample with known O_2 concentration.

c) Peak absorption cross sections $\sigma_{X\text{-}a}$ and $\sigma_{X\text{-}b}$ were obtained using absorption band amplitudes from experiment A [46] and the calculated O_2 concentrations. $\sigma_{X\text{-}a}$ was additionally corrected for insufficient spectral resolution in A. It is upscaled by fwhm ratio 105/86, using luminescence $a \longrightarrow X$ transition fwhm data from the high-resolution experiment D.

Table 2. Spectral Parameters of O_2 in SiO_2 Glass and in Different Solvents: Peak Absorption Cross Sections σ of $X \rightarrow a$ (1272 nm) and $X \rightarrow b$ (765 nm) Transitions, and Radiative Decay Rates for $a \rightarrow X$ Transition.

Medium	σ(1272 nm) , (10^{-24} cm^2)	σ(765nm) (10^{-24} cm^2)	k_r^{a-X}(s^{-1})
silica glass	27[a)]	8.4[a)]	0.34[a)]
water	6[b)]	4.5[b)] 5.1[d)]	0.209[e)]
toluene	27[b)] 34.8[c)]	6.7[d)]	1.44[d,e)]
benzene	25[b)]		1.5[d,e)]
CCl_4	20[b)]	2.7[b)]	1.06[d)] 1.17[e)]
ethanol	10[b)], 17.7[c)]	4.0[b)]	0.55[d,e)]
acetone	11.5[b)], 11.5[c)]	3.7[b)]	0.56[d)] 0.543[e)]

a) This work, based on analysis of data in Refs. [18,24,25,46]

b) Ref. [14]

c) Ref. [49]

d) Ref. [11]

e) Ref. [5]

References

(1) Jarvi, M. T.; Niedre, M. J.; Patterson, M. S.; Wilson, B. C. Singlet Oxygen Luminescence Dosimetry (SOLD) for Photodynamic Therapy: Current Status, Challenges and Future Prospects. *Photochem. Photobiol.* **2006**, *82* (5), 1198. https://doi.org/10.1562/2006-05-03-IR-891.

(2) Li, B.; Lin, L.; Lin, H.; Wilson, B. C. Photosensitized Singlet Oxygen Generation and Detection: Recent Advances and Future Perspectives in Cancer Photodynamic Therapy. *J. Biophotonics* **2016**, *9* (11–12), 1314–1325. https://doi.org/10.1002/jbio.201600055.

(3) van Straten, D.; Mashayekhi, V.; de Bruijn, H.; Oliveira, S.; Robinson, D.; van Straten, D.; Mashayekhi, V.; de Bruijn, H. S.; Oliveira, S.; Robinson, D. J. Oncologic Photodynamic Therapy: Basic Principles, Current Clinical Status and Future Directions. *Cancers* **2017**, *9* (2), 19. https://doi.org/10.3390/cancers9020019.

(4) Nosaka, Y.; Nosaka, A. Y. Generation and Detection of Reactive Oxygen Species in Photocatalysis. *Chem. Rev.* **2017**, *117* (17), 11302–11336. https://doi.org/10.1021/acs.chemrev.7b00161.

(5) Schweitzer, C.; Schmidt, R. Physical Mechanisms of Generation and Deactivation of Singlet Oxygen. *Chem. Rev.* **2003**, *103* (5), 1685–1758. https://doi.org/10.1021/cr010371d.

(6) Krasnovsky Jr., A. A. Luminescence and Photochemical Studies of Singlet Oxygen Photonics. *J. Photochem. Photobiol. Chem.* **2008**, *196* (2–3), 210–218. https://doi.org/10.1016/j.jphotochem.2007.12.015.

(7) *Singlet Oxygen: Applications in Biosciences and Nanosciences, Volume 1*, 1 edition.; Nonell, S., Flors, C., Eds.; Comprehensive Series in Photochemical & Photobiological Sciences; Royal Society of Chemistry: Cambridge, 2016.

(8) Skuja, L.; Güttler, B.; Schiel, D.; Silin, A. R. Infrared Photoluminescence of Preexisting or Irradiation-Induced Interstitial Oxygen Molecules in Glassy SiO_2 and α-Quartz. *Phys. Rev. B* **1998**, *58* (21), 14296–14304. https://doi.org/10.1103/PhysRevB.58.14296.

(9) Agnello, S.; Cannas, M.; Vaccaro, L.; Vaccaro, G.; Gelardi, F. M.; Leone, M.; Militello, V.; Boscaino, R. Near-Infrared Emission of O_2 Embedded in Amorphous SiO_2 Nanoparticles. *J. Phys. Chem. C* **2011**, *115* (26), 12831–12835. https://doi.org/10.1021/jp2035554.

(10) Kajihara, K.; Skuja, L.; Hosono, H. Diffusion and Reactions of Photoinduced Interstitial Oxygen Atoms in Amorphous SiO_2 Impregnated with ^{18}O-Labeled Interstitial Oxygen Molecules. *J. Phys. Chem. C* **2014**, *118* (8), 4282–4286. https://doi.org/10.1021/jp412606a.

(11) Bregnhøj, M.; Westberg, M.; Minaev, B. F.; Ogilby, P. R. Singlet Oxygen Photophysics in Liquid Solvents: Converging on a Unified Picture. *Acc. Chem. Res.* **2017**, *50* (8), 1920–1927. https://doi.org/10.1021/acs.accounts.7b00169.

(12) Minaev, B. F. Spin-Orbit Coupling Mechanism of Singlet Oxygen $a^1{}_g$ Quenching by Solvent Vibrations. *Chem. Phys.* **2017**, *483–484*, 84–95. https://doi.org/10.1016/j.chemphys.2016.11.012.

(13) Jockusch, S.; Turro, N. J.; Thompson, E. K.; Gouterman, M.; Callis, J. B.; Khalil, G. E. Singlet Molecular Oxygen by Direct Excitation. *Photochem Photobiol Sci* **2008**, *7* (2), 235– 239. https://doi.org/10.1039/B714286B.

(14) Krasnovsky, A. A.; Kozlov, A. S. Photonics of Dissolved Oxygen Molecules. Comparison of the Rates of Direct and Photosensitized Excitation of Oxygen and Reevaluation of the Oxygen Absorption Coefficients. *J. Photochem. Photobiol. Chem.* **2016**, *329*, 167–174. https://doi.org/10.1016/j.jphotochem.2016.06.026.

(15) Bregnhøj, M.; Krægpøth, M. V.; Sørensen, R. J.; Westberg, M.; Ogilby, P. R. Solvent and Heavy-Atom Effects on the $O_2(X^3\Sigma_g^-) \rightarrow O_2(b^1\Sigma_g^+)$ Absorption Transition. *J. Phys. Chem. A* **2016**, *120* (42), 8285–8296. https://doi.org/10.1021/acs.jpca.6b08035.

(16) Bregnhøj, M.; Rodal-Cedeira, S.; Pastoriza-Santos, I.; Ogilby, P. R. Light Scattering versus Plasmon Effects: Optical Transitions in Molecular Oxygen near a Metal Nanoparticle. *J. Phys. Chem. C* **2018**, *122* (27), 15625–15634. https://doi.org/10.1021/acs.jpcc.8b03387.

(17) Skuja, L.; Kajihara, K.; Hirano, M.; Hosono, H. Oxygen-Excess-Related Point Defects in Glassy/Amorphous SiO_2 and Related Materials. *Nucl. Instrum. Methods Phys. Res. Sect. B Beam Interact. Mater. At.* **2012**, *286*, 159–168. https://doi.org/10.1016/j.nimb.2012.02.038.

(18) Carvalho, W.; Dumas, P.; Corset, J.; Neuman, V. Raman Spectra and Oxygen-Related Absorption Bands in Pure Silica Core Fibres. *J. Raman Spectrosc.* **1985**, *16* (5), 330–331. https://doi.org/10.1002/jrs.1250160510.

(19) Kajihara, K.; Kamioka, H.; Hirano, M.; Miura, T.; Skuja, L.; Hosono, H. Interstitial Oxygen Molecules in Amorphous SiO2. III. Measurements of Dissolution Kinetics, Diffusion

Coefficient, and Solubility by Infrared Photoluminescence. *J. Appl. Phys.* **2005**, *98* (1), 013529. https://doi.org/10.1063/1.1943506.

(20) Lancry, M.; Poumellec, B.; Canning, J.; Cook, K.; Poulin, J.-C.; Brisset, F. Ultrafast Nanoporous Silica Formation Driven by Femtosecond Laser Irradiation: In the Heart of Nanogratings. *Laser Photonics Rev.* **2013**, *7* (6), 953–962. https://doi.org/10.1002/lpor.201300043.

(21) Redkov, A. V.; Melehin, V. G.; Lipovskii, A. A. How Does Thermal Poling Produce Interstitial Molecular Oxygen in Silicate Glasses? *J. Phys. Chem. C* **2015**, *119* (30), 17298– 17307. https://doi.org/10.1021/acs.jpcc.5b04513.

(22) Skuja, L.; Kajihara, K.; Hirano, M.; Hosono, H. Crucial Dependence of Excimer Laser Toughness of "Wet" Silica on Excess Oxygen. *J. Non-Cryst. Solids* **2011**, *357* (8–9), 1875– 1878. https://doi.org/10.1016/j.jnoncrysol.2010.12.047.

(23) Kashaykin, P. F.; Tomashuk, A. L.; Salgansky, M. Y.; Abramov, A. N.; Iskhakova, L. D.; Lobanov, N. S.; Nishchev, K. N.; Guryanov, A. N.; Dianov, E. M. Silica Optical Fibers with High Oxygen Excess in the Core: A New Type of Radiation-Resistant Fiber. *Proc. SPIE* **2015**, *9507*, 950705(1-9). https://doi.org/10.1117/12.2087317.

(24) Skuja, L.; Güttler, B.; Schiel, D.; Silin, A. R. Quantitative Analysis of the Concentration of Interstitial O_2 Molecules in SiO_2 Glass Using Luminescence and Raman Spectrometry. *J. Appl. Phys.* **1998**, *83* (11), 6106–6110. https://doi.org/10.1063/1.367480.

(25) Kajihara, K.; Hirano, M.; Uramoto, M.; Morimoto, Y.; Skuja, L.; Hosono, H. Interstitial Oxygen Molecules in Amorphous SiO_2. I. Quantitative Concentration Analysis by Thermal Desorption, Infrared Photoluminescence, and Vacuum-Ultraviolet Optical Absorption. *J. Appl. Phys.* **2005**, *98* (1), 013527(1-6). https://doi.org/10.1063/1.1943504.

(26) Kajihara, K.; Kamioka, H.; Hirano, M.; Miura, T.; Skuja, L.; Hosono, H. Interstitial Oxygen Molecules in Amorphous SiO_2. II. The Influence of Common Dopants (SiOH, SiF, and SiCl Groups) and Fictive Temperature on the Decay of Singlet Photoluminescence. *J. Appl. Phys.* **2005**, *98* (1), 013528. https://doi.org/10.1063/1.1943505.

(27) Schmidt, R.; Afshari, E. Collisional Deactivation of $O_2(^1{}_g)$ by Solvent Molecules. Comparative Experiments with $^{16}O_2$ and $^{18}O_2$. *Berichte Bunsenges. Für Phys. Chem.* **1992**, *96* (6), 788–794. https://doi.org/10.1002/bbpc.19920960610.

(28) Lee, P. C.; Rodgers, M. A. J. Kinetic Properties of Singlet Oxygen in a Polymeric Microheterogeneous System. *J. Phys. Chem.* **1984**, *88* (19), 4385–4389. https://doi.org/10.1021/j150663a040.

(29) Jockusch, S.; Sivaguru, J.; Turro, N. J.; Ramamurthy, V. Direct Measurement of the Singlet Oxygen Lifetime in Zeolites by Near-IR Phosphorescence. *Photochem. Photobiol. Sci.* **2005**, *4* (5), 403–405. https://doi.org/10.1039/b501701g.

(30) Zanatta, M.; Baldi, G.; Brusa, R. S.; Egger, W.; Fontana, A.; Gilioli, E.; Mariazzi, S.; Monaco, G.; Ravelli, L.; Sacchetti, F. Structural Evolution and Medium Range Order in Permanently Densified Vitreous SiO_2. *Phys. Rev. Lett.* **2014**, *112* (4). https://doi.org/10.1103/PhysRevLett.112.045501.

(31) Steinert, S.; Ziem, F.; Hall, L. T.; Zappe, A.; Schweikert, M.; Götz, N.; Aird, A.; Balasubramanian, G.; Hollenberg, L.; Wrachtrup, J. Magnetic Spin Imaging under Ambient Conditions with Sub-Cellular Resolution. *Nat. Commun.* **2013**, *4* (1). https://doi.org/10.1038/ncomms2588.

(32) Lakowicz, J. R. *Principles of Fluorescence Spectroscopy*, Third edition.; Springer New York, 2006.

(33) Kresse, G.; Joubert, D. From Ultrasoft Pseudopotentials to the Projector Augmented-Wave Method. *Phys. Rev. B* **1999**, *59* (3), 1758–1775. https://doi.org/10.1103/PhysRevB.59.1758.

(34) Kresse, G.; Hafner, J. Ab Initio Molecular Dynamics for Liquid Metals. *Phys. Rev. B* **1993**, *47* (1), 558–561. https://doi.org/10.1103/PhysRevB.47.558.

(35) Perdew, J. P.; Burke, K.; Ernzerhof, M. Generalized Gradient Approximation Made Simple. *Phys. Rev. Lett.* **1996**, *77* (18), 3865–3868. https://doi.org/10.1103/PhysRevLett.77.3865.

(36) Blöchl, P. E. Projector Augmented-Wave Method. *Phys. Rev. B* **1994**, *50* (24), 17953–17979. https://doi.org/10.1103/PhysRevB.50.17953.

(37) Poulsen, T. D.; Ogilby, P. R.; Mikkelsen, K. V. Polarizabilities of the First Excited (AΔg) and Ground (X3) States of Molecular Oxygen. *J. Phys. Chem. A* **1998**, *102* (45), 8970–8973. https://doi.org/10.1021/jp981925s.

(38) Sharipov, A. S.; Loukhovitski, B. I.; Pelevkin, A. V.; Kobtsev, V. D.; Kozlov, D. N. Polarizability of Electronically Excited Molecular Oxygen: Theory and Experiment. *J. Phys. B At. Mol. Opt. Phys.* **2019**, *52* (4), 045101. https://doi.org/10.1088/1361-6455/aaf9d9.

(39) Bongiorno, A.; Pasquarello, A. Oxygen Diffusion through the Disordered Oxide Network during Silicon Oxidation. *Phys. Rev. Lett.* **2002**, *88* (12), 125901. https://doi.org/10.1103/PhysRevLett.88.125901.

(40) Bongiorno, A.; Pasquarello, A. Multiscale Modeling of Oxygen Diffusion through the Oxide during Silicon Oxidation. *Phys. Rev. B* **2004**, *70* (19), 195312(1-14). https://doi.org/10.1103/PhysRevB.70.195312.

(41) Alkauskas, A.; Broqvist, P.; Pasquarello, A. Charge State of the O_2 Molecule during Silicon Oxidation through Hybrid Functional Calculations. *Phys. Rev. B* **2008**, *78* (16), 161305. https://doi.org/10.1103/PhysRevB.78.161305.

(42) Hartwig, C. M.; Vitko, J. Raman Spectroscopy of Molecular Hydrogen and Deuterium Dissolved in Vitreous Silica. *Phys. Rev. B* **1978**, *18* (7), 3006–3014. https://doi.org/10.1103/PhysRevB.18.3006.

(43) Agnello, S.; Vaccaro, L.; Cannas, M.; Kajihara, K. Temperature Dependence of O_2 Singlet Photoluminescence in Silica Nanoparticles. *J. Non-Cryst. Solids* **2013**, *379*, 220–223. https://doi.org/10.1016/j.jnoncrysol.2013.08.016.

(44) Jensen, R. L.; Holmegaard, L.; Ogilby, P. R. Temperature Effect on Radiative Lifetimes: The Case of Singlet Oxygen in Liquid Solvents. *J. Phys. Chem. B* **2013**, *117* (50), 16227–16235. https://doi.org/10.1021/jp410185n.

(45) Kajihara, K.; Miura, T.; Kamioka, H.; Hirano, M.; Skuja, L.; Hosono, H. Isotope Effect on the Infrared Photoluminescence Decay of Interstitial Oxygen Molecules in Amorphous SiO $_2$. *Appl. Phys. Express* **2009**, *2*, 056502. https://doi.org/10.1143/APEX.2.056502.

(46) Heitmann, W.; Bonewitz, H. U.; Mühlich, A. New Absorption Bands in Pure and F-Doped Silica Optical Fibres. *Electron. Lett.* **1983**, *19* (16), 616–617. https://doi.org/10.1049/el:19830420.

(47) Di Francesca, D.; Girard, S.; Agnello, S.; Marcandella, C.; Paillet, P.; Boukenter, A.; Gelardi, F. M.; Ouerdane, Y. Near Infrared Radio-Luminescence of O $_2$ Loaded Radiation Hardened Silica Optical Fibers: A Candidate Dosimeter for Harsh Environments. *Appl. Phys. Lett.* **2014**, *105* (18), 183508. https://doi.org/10.1063/1.4901340.

(48) Feofilov, P. P. *The Physical Basis of Polarized Emission*; Consultants Bureau: New York, 1961.

(49) Sivéry, A.; Anquez, F.; Pierlot, C.; Aubry, J. M.; Courtade, E. Singlet Oxygen ($^1O_2$) Generation upon 1270nm Laser Irradiation of Ground State Oxygen ($^3O_2$) Dissolved in Organic Solvents: Simultaneous and Independent Determination of $^1O_2$ Production Rate and

Reactivity with Chemical Traps. *Chem. Phys. Lett.* **2013**, *555*, 252–257. https://doi.org/10.1016/j.cplett.2012.10.063.

Table of Contents Image

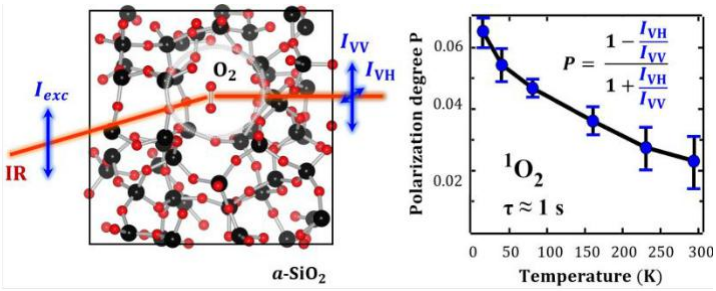

Institute of Solid State Physics, University of Latvia as the Center of Excellence has received funding from the European Union's Horizon 2020 Framework Programme H2020-WIDESPREAD-01-2016-2017-TeamingPhase2 under grant agreement No. 739508, project CAMART²